Fully coupled six-dimensional calculations of the water dimer vibration-rotation-tunneling states with a split Wigner pseudo spectral approach

Claude Leforestier
Laboratoire Structure et Dynamique des Systèmes Moléculaires et Solides (UMR 5636), CC 014, Université des Sciences et Techniques du Languedoc, 34095 Montpellier Cédex 05, France

Linda B. Braly, Kun Liu, Matthew J. Elrod,[a] and Richard J. Saykally
Department of Chemistry, University of California, Berkeley, California 94720-1460

A novel and efficient pseudospectral method for performing fully coupled six-dimensional bound state dynamics calculations is presented, including overall rotational effects. A Lanczos based iterative diagonalization scheme produces the energy levels in increasing energies. This scheme, which requires repetitively acting the Hamiltonian operator on a vector, circumvents the problem of constructing the full matrix. This permits the use of ultralarge molecular basis sets (up to over one million states for a given symmetry) in order to fully converge the calculations. The Lanczos scheme was conducted in a symmetry adapted spectral representation, containing Wigner functions attached to each monomer. The Hamiltonian operator has been split into different terms, each corresponding to an associated diagonal or nearly diagonal representation. The potential term is evaluated by a pseudospectral scheme of Gaussian accuracy, which guarantees the variational principle. Spectroscopic properties are computed with this method for four of the most widely used water dimer potentials, and compared against recent terahertz laser spectroscopy results. Comparisons are also made with results from other dynamics methods, including quantum Monte Carlo (QMC) and reversed adiabatic approximation calculations. None of the potential surfaces produces an acceptable agreement with experiments. While QMC methods yield good results for ground (nodeless) states, they are highly inaccurate for excited states. © *1997 American Institute of Physics.* [S0021-9606(97)01020-9]

I. INTRODUCTION

While the study of intermolecular forces has a very long history, tremendous progress in our understanding of the details of molecular interactions has been achieved in the last several years.[1–4] This has occurred because of major and simultaneous advances in high resolution spectroscopy of weakly bound clusters,[1,2] *ab initio* calculations of intermolecular potential surfaces (IPS),[5] and in the theoretical methods used to describe the dynamics that occur on the IPS.[1,3,6] These advances have now permitted the direct determination of accurate and detailed IPS for systems with two, three, and four fully coupled degrees of freedom.

These potential surface determinations have generally proceeded via direct least squares fits of far-IR and mid-IR vibration-rotation-tunneling (VRT) and microwave spectra, which were constrained with other available data (multipole moments, dispersion coefficients, virial coefficients,...). In order to perform such calculations for systems with 3 or more coupled degrees of freedom, accurate and very efficient dynamics methods must be employed, since a nonlinear regression analysis will typically involve ~ 100 calls to the algorithm which calculates the spectra from the IPS. If one employs a variational method with an $\mathscr{L}^2$ finite basis representation (FBR), it is generally found that at least 10 basis functions per degree of freedom are required for spectroscopy accuracy. In order to calculate VRT spectra from an IPS for the general case of two interacting linear molecules with frozen internal motions (usually a very good approximation), this necessitates the solution of an eigenvalue problem of dimension 10^4. Elrod and Saykally[1] employed such an $\mathscr{L}^2$ approach in their determination of the four-dimensional (4D) IPS of $(HCl)_2$, but upon extending this approach to the six-dimensional (6D) case of two interacting polyatomics both CPU time requirements ($\propto N^3$) and storage demands ($\propto N^2$) thus become prohibitive. Nevertheless, a most impressive demonstration of $\mathscr{L}^2$ variational method was recently presented by van der Avoird and co-workers, in which an empirical potential model was employed to quantitatively reproduce all measured properties of the ammonia dimer (microwave and VRT spectra, dipole moments, nuclear quadrupole splittings of the $(NH_3)_2$ and $(ND_3)_2$ isotopomers.[7] However, the considerable expense of this calculation still precludes a rigorous determination of the IPS through regression analysis.

A number of innovative approaches to this problem have appeared recently. The collocation method,[8–10] used for the determination of the three-dimensional (3D) $Ar–H_2O$[11,12] and $Ar–NH_3$[13] potentials, yields very simple programming and essentially complete generality with respect to the form of the potential and basis functions, but suffers from the

Acceptor Tunneling

Geared Donor-Acceptor Interchange Tunneling
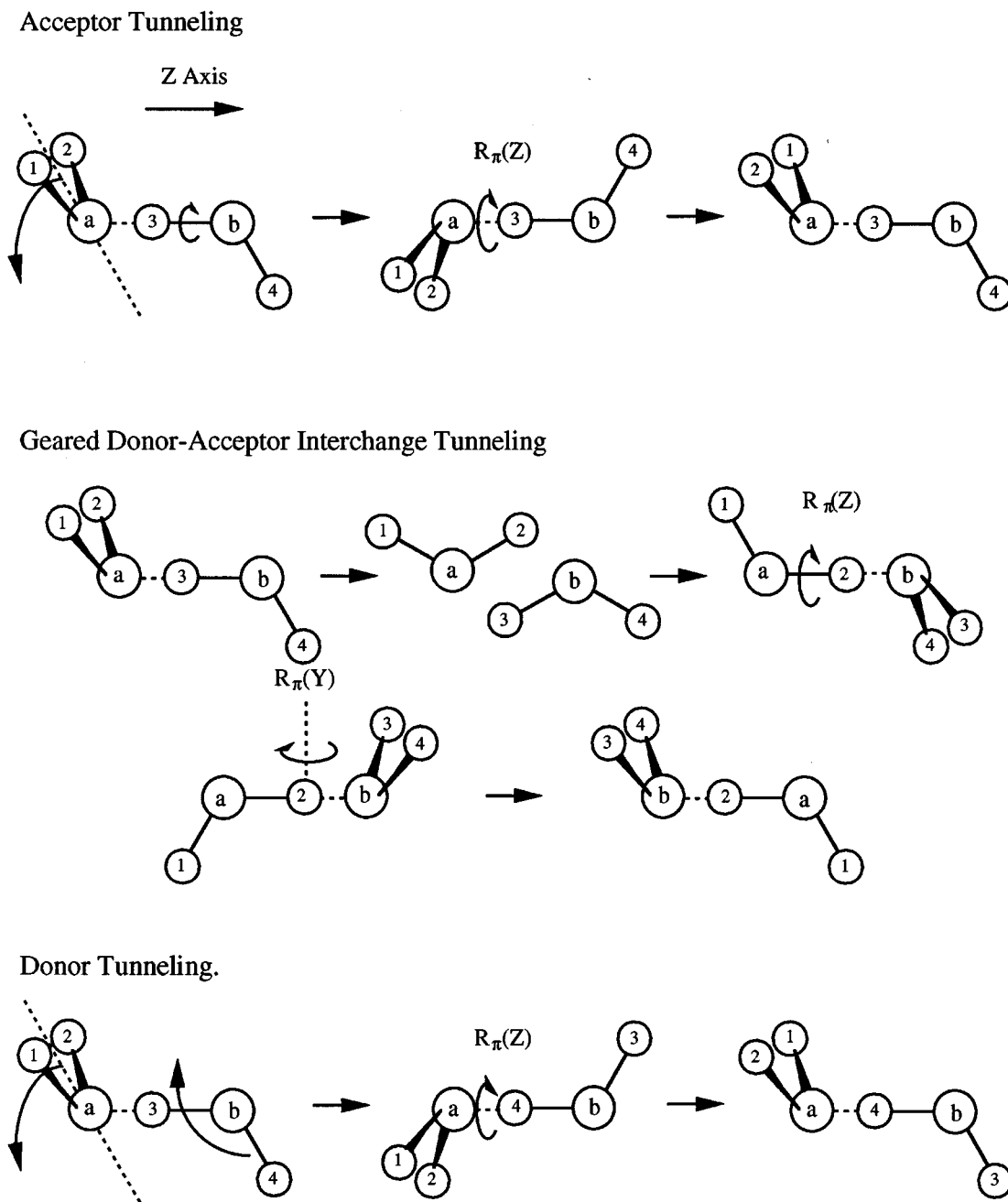

Donor Tunneling.

FIG. 1. The three internal tunneling pathways giving rise to energy level splittings, as discussed in the text.

computational inefficiency associated with the non-symmetric eigenvalue problem. Quantum Monte Carlo (QMC) methods developed so far[14–18] offer a convenient and efficient extension to larger systems. A recent demonstration of the power of this method was presented by Liu *et al.*[4] wherein a fully coupled 30D treatment of the VRT dynamics in the water hexamer with diffusion quantum Monte Carlo (DQMC) using Stone's ASP potential model produced excellent agreement for ground state (nodeless) properties with far-IR laser spectroscopy results. Such QMC methods suffer from a great difficulty in treating excited states, however,

and this limits their usage for potential surface determinations.

The method we describe in the present paper consists in a Lanczos based, split Hamiltonian formulation of the problem. Initiated by Feit and Fleck[19,20] and Kosloff and Kosloff,[21,22] the split Hamiltonian method makes use of two different representations associated with the Hamiltonian operator. In its original formulation, the kinetic energy part was evaluated in the spectral representation (plane waves), while a grid was used for the potential. It should be noted that these two representations are equivalent, being related by a unitary

TABLE I. Water dimer parameters used in the calculations.

$R_{O-H} = 1.808846$ a.u.	$\widehat{HOH} = 104.5°$	$\mu_{H_2O,H_2O} = 9.00525$ a.m.u
$B_x = 14.5216$ cm^{-1}	$B_y = 9.2778$ cm^{-1}	$B_z = 27.8806$ cm^{-1}

transform [multidimensional fast Fourier transform (FFT)]. Such a split representation has been confined for many years to iterative time dependent propagation methods (see Ref. 23 for a review). It was later introduced in bound states calculations by Friesner *et al.*[24] through the adiabatic pseudospectral (APS) method. The scheme, based on the iterative Lanczos method has been applied to the simulation of SEP spectra. In this formulation, the spectral representation consisted of the adiabatic eigenstates $\{\Phi_n(\mathbf{q};\theta_\alpha)\}$ with respect to some slow coordinate θ:

$$\mathbf{H}(\theta_\alpha)\Phi_n(\mathbf{q};\theta_\alpha) = \mathscr{E}_n(\theta_\alpha)\Phi_n(\mathbf{q};\theta_\alpha). \tag{1}$$

These adiabatic states were computed on a two-dimensional grid $\mathbf{q}_p$ by means of the successive adiabatic reduction (SAR) method of Bačić and Light,[25,26] and were used in the treatment of Friesner *et al.* to perform the spectral to grid transformation using the collocation matrices

$$\mathbf{R}_{pn}^{(\alpha)} = \Phi_n(\mathbf{q}_p;\theta_\alpha). \tag{2}$$

This grid representation was then used in order to evaluate some residual terms of the Hamiltonian operator (nonadiabatic coupling terms). Finally, the effect of these terms was expressed in the spectral representation by means of the inverse grid to spectral representation

$$\mathscr{R}^{-1} = [\mathbf{R}^+ \cdot \mathbf{R}]^{-1} \cdot \mathbf{R}^+ \tag{3}$$

defined by least squares fitting.

The innovative aspect of this method is that of using a contracted spectral representation as the primary one. From a numerical point of view, a contracted representation is much more efficient as it is associated with a narrower spectrum, compared to an uncontracted one. This property is of utmost importance as it governs the convergence properties of the subsequent iterative (Lanczos) eigenstates calculation. Another consequence of using such a contracted basis is that it ensures converged matrix elements of the Hamiltonian op-

TABLE II. Symmetry adapted linear combination vectors for to the different irreducible representations Γ. λ is defined as $J + j_A + j_B$.

$|\xi_1,\Omega\rangle$	$|j_A j_B k_A k_B ; j\Omega\rangle$	
$|\xi_2,\Omega\rangle$	$|j_B j_A k_B k_A ; j\bar{\Omega}\rangle$	
$|\xi_3,\Omega\rangle$	$|j_A j_B \bar{k}_A \bar{k}_B ; j\bar{\Omega}\rangle$	
$|\xi_4,\Omega\rangle$	$|j_B j_A \bar{k}_A \bar{k}_A ; j\Omega\rangle$	
Γ	$|j_A j_B k_A k_B ; j\Omega,\Gamma\rangle$	(k_A,k_B) parity
A_1^+	$\xi_1 + (-1)^\lambda \xi_2 + (-1)^{\lambda+j}\xi_3 + (-1)^j \xi_4$	e e
A_2^+	$\xi_1 - (-1)^\lambda \xi_2 + (-1)^{\lambda+j}\xi_3 - (-1)^j \xi_4$	o e
B_1^+	$\xi_1 - (-1)^\lambda \xi_2 + (-1)^{\lambda+j}\xi_3 - (-1)^j \xi_4$	e e
B_2^+	$\xi_1 + (-1)^\lambda \xi_2 + (-1)^{\lambda+j}\xi_3 + (-1)^j \xi_4$	o o
E^+	$\xi_1 + (-1)^{\lambda+j}\xi_3$	o e or eo
	$\xi_2 + (-1)^{\lambda+j}\xi_4$	o e or eo
A_1^-	$\xi_1 + (-1)^\lambda \xi_2 - (-1)^{\lambda+j}\xi_3 - (-1)^j \xi_4$	e e
A_2^-	$\xi_1 - (-1)^\lambda \xi_2 - (-1)^{\lambda+j}\xi_3 + (-1)^j \xi_4$	o e
B_1^-	$\xi_1 - (-1)^\lambda \xi_2 - (-1)^{\lambda+j}\xi_3 + (-1)^j \xi_4$	e e
B_2^-	$\xi_1 + (-1)^\lambda \xi_2 - (-1)^{\lambda+j}\xi_3 - (-1)^j \xi_4$	o o
E^-	$\xi_1 - (-1)^{\lambda+j}\xi_3$	o e or eo
	$\xi_2 - (-1)^{\lambda+j}\xi_4$	o e or eo

erator. As discussed by Friesner,[27] the inverse transform [Eq. 3] allows one to eliminate the aliasing terms associated with evaluating the residual terms on a grid. One thus regains the variational principle which is otherwise lost. This approach has been recently generalized and applied to tetra-atomic systems.[28]

The next step in the development of using contracted basis sets in split Hamiltonian algorithms is due to Corey and colleagues. In a very important paper, Corey and Lemoine[29] had shown how one can transform between a spherical harmonics basis set and a two-dimensional grid associated with the polar angles. The key point of this transformation is that it treats exactly the apparent singularity of the kinetic energy operator ($\sin^{-2}\theta \partial^2/\partial\varphi^2$) that appears in a pure grid description. As a result, the spectrum of the kinetic energy operator displays the smallest possible range. This paper established an efficient handling of a multidimensional grid associated with general non-direct product basis sets. The essential departure from Light's original formulation[30] is that one no longer seeks a unitary transform between the two representations. As a result, the two representations are no longer equivalent, the spectral representation becoming the primary one as it is more compact.[31–35]

Recently the split Hamiltonian method has been applied by one of us (C.L.)[32] to the computation of the VRT states of the Ar–H_2O van der Waals complex. The key feature of the calculation was the definition of a grid associated with a basis of Wigner functions, similar in spirit to Corey and Lemoine's approach for spherical harmonics.[29] It consists of a Jacobi transform followed by a double Fourier transform. In order to maintain the variational principle within the scheme, care has been taken to remove the aliasing terms resulting from evaluating the potential on a grid. This has been realized by using a grid size significantly larger than the spectral representation dimension. When combined with the Lanczos algorithm[36,37] for extracting the low lying eigenstates, this split Wigner pseudospectral (SWPS) method was
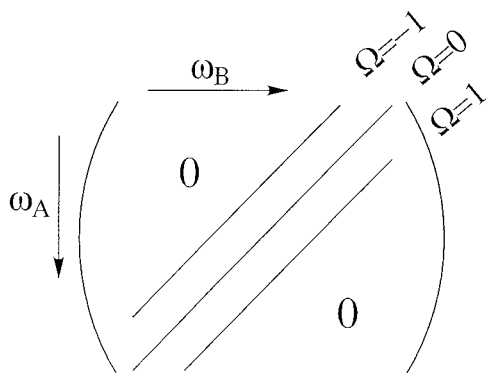

FIG. 2. Structure of the wave function (ω_A,ω_B)-components in the uncoupled basis set $\mathscr{B}_{unc}$ for a total angular momentum value $J=1$.

TABLE III. $J=0$ energy levels obtained from a 5D calculation using the Clementi and coworkers surface. The interfragment distance R_* was set to 5.6242 a.u. Wigner basis sets corresponding to $j_{max}=11$ have been used on each monomer. Figures in parentheses correspond to the energy change in the level position associated with an increase in the basis set size from $j_{max}-1$ to its actual value of j_{max}.

	B_1^+ ———	12.21 (−0.09)
	E^+ ———	4.36 (−0.04)
+152.26 (−0.09)	A_1^+ ———	
	B_2^- ———	10.79 (−0.02)
	E^- ———	8.28 (−0.00)
+151.37 (−0.13)	A_2^- ———	
	A_1^- ———	7.32 (−0.00)
	E^- ———	0.04 (−0.01)
+149.50 (−0.08)	B_1^- ———	
	A_2^+ ———	6.76 (+0.02)
	E^+ ———	2.78 (+0.03)
+133.27 (−0.07)	B_2^+ ———	
	B_1^- ———	1.86 (−0.04)
	E^- ———	0.83 (−0.05)
+111.75 (−0.09)	A_1^- ———	
	B_2^- ———	2.69 (−0.00)
	E^- ———	1.60 (+0.07)
+96.50 (−0.09)	A_2^- ———	
	B_1^+ ———	5.62 (−0.02)
	E^+ ———	3.17 (+0.03)
+81.18 (−0.08)	A_1^+ ———	
	A_2^+ ———	1.41 (−0.16)
	E^+ ———	0.45 (−0.08)
+75.03 (+0.02)	B_2^+ ———	
	B_2^- ———	1.25 (−0.00)
	E^- ———	0.66 (+0.01)
+12.48 (−0.02)	A_2^- ———	
	B_1^+ ———	1.26 (+0.01)
	E^+ ———	0.79 (−0.02)
−1113.31 (−0.17)	A_1^+ ———	

TABLE IV. Same as Table III for the RWK2 surface. A j_{max} value of 13 has been used for each monomer.

	B_2^- ———	10.81 (−0.16)
	E^- ———	0.54 (−0.02)
+188.74 (+0.00)	A_2^- ———	
	B_1^+ ———	0.21 (+0.00)
	E^+ ———	0.18 (+0.00)
+171.84 (−0.02)	A_1^+ ———	
	A_1^- ———	0.15 (−0.02)
	B_1^- ———	0.07 (−0.01)
+168.54 (−0.08)	E^- ———	
	A_2^+ ———	0.27 (+0.00)
	E^+ ———	0.09 (−0.02)
+158.17 (+0.01)	B_2^+ ———	
	B_1^- ———	0.13 (−0.01)
	E^- ———	0.01 (−0.01)
+125.53 (+0.02)	A_1^- ———	
	B_2^- ———	0.09 (+0.01)
	E^- ———	0.09 (−0.02)
+108.00 (+0.01)	A_2^- ———	
	B_1^+ ———	0.44 (+0.00)
	E^+ ———	0.29 (−0.01)
+107.45 (+0.01)	A_1^+ ———	
	A_2^+ ———	0.04 (−0.02)
	E^+ ———	0.01 (+0.02)
+58.82 (−0.01)	B_2^+ ———	
	E^- ———	0.06 (+0.01)
	B_2^- ———	0.04 (+0.00)
+27.50 (+0.00)	A_2^- ———	
	E^+ ———	0.10 (+0.02)
	B_1^+ ———	0.04 (+0.00)
−1305.65 (−0.04)	A_1^+ ———	

shown to be both very efficient and versatile with respect to the form of the potential, as well has having minimal storage requirements.

In the present paper we describe the application of the SWPS method to the calculation of VRT spectra of the 6D water dimer system. With this approach, we are able to *quantitatively* evaluate several widely used IPS for the water dimer with respect to their ability to reproduce high precision VRT spectra recently measured with far infrared laser methods, as well as ground state microwave spectra.

There are a maximum of 16 equivalent structures of the water dimer that can be generated without breaking any chemical bond.[38] The dimer tunnels along low-energy barrier pathways on the IPS to access the different structures. Permutation of the nuclei gives rise to 8 equivalent structures. Inversion of these structures through the center of mass gen-

erates 8 more configurations. If the equilibrium structure contains a plane of symmetry, as the evidence currently supports, then there are only 8 distinct configurations. The permutation inversion (PI) symmetry group G_{16} is typically used to explain the resulting splittings in the rovibrational levels. G_{16} is isomorphic with the $D_{4h}(M)$ point group and is consistent with observed VRT dynamics. For further discussion of the water dimer group theory see References 38–40.

Acceptor tunneling has the lowest energy barrier making it the most feasible tunneling motion on the IPS. This motion allows for the exchange of the protons in the water molecule acting as the H-bond acceptor. Figure 1 shows the proposed pathway, but the net effect is a C_2 rotation of the acceptor about its symmetry axis. Each rovibrational energy level of the non-tunneling water dimer is split into two.

The next most feasible tunneling motion is identified as donor-acceptor interchange tunneling. There are several possible pathways with the most likely one being the geared motion shown in Fig. 1.[41] In donor-acceptor interchange, the

TABLE V. Same as Table III for the ASP1 surface. A j_{max} value of 10 has been used for each monomer.

Energy	Symmetry	Value
	B_2^- ———	16.52 (−0.17)
	E^- ———	10.81 (−0.13)
+135.20 (+0.02)	A_2^- ———	
	A_1^- ———	11.06 (−0.10)
	E^- ———	1.20 (+0.00)
+125.12 (−0.01)	B_1^- ———	
	B_1^+ ———	21.00 (−0.16)
	E^+ ———	9.45 (−0.05)
+124.54 (−0.07)	A_1^+ ———	
	A_2^+ ———	9.76 (−0.05)
	E^+ ———	3.19 (+0.02)
+115.05 (−0.11)	B_2^+ ———	
	B_1^- ———	3.65 (−0.03)
	E^- ———	2.57 (−0.11)
+103.15 (+0.03)	A_1^- ———	
	B_2^- ———	1.68 (+0.02)
	E^- ———	1.05 (−0.06)
+98.24 (−0.02)	A_2^- ———	
	B_1^+ ———	10.41 (−0.02)
	E^+ ———	7.98 (−0.07)
+83.18 (−0.02)	A_1^+ ———	
	A_2^+ ———	7.62 (−0.04)
	E^+ ———	1.81 (+0.01)
+72.88 (+0.05)	B_2^+ ———	
	B_2^- ———	1.83 (−0.01)
	E^- ———	1.07 (−0.01)
+10.60 (−0.02)	A_2^- ———	
	B_1^+ ———	2.47 (−0.01)
	E^+ ———	1.82 (+0.00)
−984.75 (−0.18)	A_1^+ ———	

TABLE VI. Same as Table III for the ASP2 surface. A j_{max} value of 10 has been used for each monomer.

Energy	Symmetry	Value
	B_1^+ ———	14.82 (−0.12)
	E^+ ———	6.86 (−0.06)
+129.22 (−0.06)	A_1^+ ———	
	E^- ———	12.60 (−0.11)
	A_1^- ———	11.90 (−0.15)
+128.19 (+0.05)	B_1^- ———	
	B_2^- ———	14.73 (−0.16)
	E^- ———	0.33 (−0.01)
+126.41 (+0.03)	A_2^- ———	
	A_2^+ ———	15.74 (−0.14)
	E^+ ———	7.57 (−0.10)
+104.45 (+0.03)	B_2^+ ———	
	E^- ———	8.94 (−0.09)
	B_2^- ———	5.20 (−0.02)
+96.88 (+0.03)	A_2^- ———	
	A_2^+ ———	3.41 (−0.01)
	E^+ ———	2.78 (+0.02)
+92.93 (−0.05)	B_2^+ ———	
	A_1^- ———	5.40 (−0.02)
	B_1^- ———	5.13 (−0.04)
+87.91 (−0.04)	E^- ———	
	B_1^+ ———	11.57 (−0.04)
	E^+ ———	5.64 (−0.08)
+86.09 (+0.08)	A_1^+ ———	
	B_2^- ———	3.49 (−0.03)
	E^- ———	1.69 (−0.01)
+4.60 (−0.01)	A_2^- ———	
	B_1^+ ———	4.00 (−0.03)
	E^+ ———	3.11 (−0.03)
−1050.63 (−0.18)	A_1^+ ———	

roles of the individual donor and acceptor water molecules are swapped. The effect is to split the energy levels into three, but by a much smaller degree than that of acceptor tunneling. These two tunneling motions resolve all degeneracies in the water dimer.

The final rearrangement identified is that of donor tunneling wherein the H-bond donor permutes its protons. The barrier to this motion is relatively high and results in a small shift of the energy levels, but causes no further splitting.

The water dimer has been the subject of a large number of experimental and theoretical studies. High resolution microwave,[42,38,43–51] mid-IR,[52–55] and far-IR[56–59,39] spectra have all been measured. From these investigations, the hydrogen bond tunneling dynamics occurring in low K levels of the ground state and the first excited acceptor bending state are well characterized,[58,60] and several other intermolecular vibrations have recently been measured and partially analyzed.[61] Several different dynamical methods have recently been employed to calculate the VRT states corresponding to a variety of IPS that have been determined for this system. Lewerentz and Watts[62] have used QMC to calculate the tunneling splittings and intermolecular vibrations on the RWK2 surface,[63] while Gregory and Clary[64] used a DQMC method to calculate ground state structural properties with the RWK2, ASP1 and ASP2[65] surfaces. Althorpe and Clary[66] employed the reversed adiabatic approximation (RAA) to calculate ground state tunneling splittings and several intermolecular vibrations, using these same three IPS models in a 5D approximation to the coupled dynamics. These authors[67] later presented a novel DVR scheme for multidimensional dynamics calculations, and also applied it to the water dimer VRT dynamics, but again using a 5D fixed R approximation. In addition to these explicit calculations of the VRT dynamics, a large number of *ab initio* calculations have addressed this system (see Refs. 68, 69 and references cited therein), generally calculating the minimum energy structures with harmonic frequencies and intensities, but one study[68] also calculated barriers for the three distinct tunneling pathways for degenerate structural rearrangements.

In this paper, we present converged fully coupled 6D

TABLE VII. $J=0$ energy levels obtained from a 5D calculation on the Clementi and coworkers surface using $j_{max}=11$ and different k_{max} values for the Wigner basis set attached to each monomer.

	$k_{max}=11$			$k_{max}=9$			$k_{max}=7$	
	B_2^- ——	2.69		B_2^- ——	2.70		B_2^- ——	2.70
	E^- ——	1.60		E^- ——	1.61		E^- ——	1.90
$+96.50$	A_2^- ——		$+96.49$	A_2^- ——		$+96.19$	A_2^- ——	
	B_1^+ ——	5.62		B_1^+ ——	5.62		B_1^+ ——	5.69
	E^+ ——	3.17		E^+ ——	3.17		E^+ ——	2.95
$+81.18$	A_1^+ ——		$+81.19$	A_1^+ ——		$+81.23$	A_1^+ ——	
	A_2^+ ——	1.41		A_2^+ ——	1.41		A_2^+ ——	1.41
	E^+ ——	0.45		E^+ ——	0.46		E^+ ——	0.64
$+75.03$	B_2^+ ——		$+75.02$	B_2^+ ——		$+74.66$	B_2^+ ——	
	B_2^- ——	1.25		B_2^- ——	1.25		B_2^- ——	1.25
	E^- ——	0.66		E^- ——	0.66		E^- ——	0.98
$+12.48$	A_2^- ——		$+12.48$	A_2^- ——		$+12.17$	A_2^- ——	
	B_1^+ ——	1.26		B_1^+ ——	1.26		B_1^+ ——	1.26
	E^+ ——	0.79		E^+ ——	0.79		E^+ ——	0.51
-1113.31	A_1^+ ——		-1113.31	A_1^+ ——		-1112.93	A_1^+ ——	

calculations of the VRT levels of the water dimer for all six intermolecular vibrations, including the tunneling sub-levels of all symmetries for both $K=0$ and $K=1$. Four of the best existing intermolecular potential surfaces were employed, namely the *ab initio* one of Clementi and co-workers[70] and the semi-empirical RWK2[63] and ASP[65] surfaces. This enables a direct comparison to be made between our exact 6D SWPS results and those from both the approximate 5D RAA treatment[66] and the 6D QMC[62] and DQMC[64,71] results, as well as with precise experimental measurements. The outline of the paper is as follows. In Sec. II, we first review the Hamiltonian operator describing the dimer, and describe the different representations used to perform the calculations.

Section III deals with convergence tests with respect to the angular basis set associated to each monomer, for the various IPS explored in this paper. In Sec. IV, we present the VRT spectra of the 6D water dimer corresponding to these different surfaces. Finally, Sec. V presents our conclusions.

II. METHOD OF CALCULATIONS

A. Hamiltonian operator

We used the Brocks *et al.* rigid rotor formulation[72] which gives the Hamiltonian, after the normalization change $\Psi \to R^{-1}\Psi$, as

TABLE VIII. $J=0$ energy levels obtained from a 5D calculation on the RWK2 surface using $j_{max}=13$ and different k_{max} values for the Wigner basis set attached to each monomer.

	$k_{max}=11$			$k_{max}=9$			$k_{max}=7$	
	E^- ——	0.09		E^- ——	0.10		E^- ——	0.53
	B_2^- ——	0.09		B_2^- ——	0.09		B_2^- ——	0.09
$+108.00$	A_2^- ——		$+107.99$	A_2^- ——		$+107.91$	A_2^- ——	
	B_1^+ ——	0.44		B_1^+ ——	0.44		B_1^+ ——	0.59
	E^+ ——	0.29		E^+ ——	0.27		A_1^+ ——	0.15
$+107.45$	A_1^- ——		$+107.45$	A_1^- ——		$+107.66$	E^- ——	
	A_2^+ ——	0.04		A_2^+ ——	0.03		E^+ ——	0.38
	E^+ ——	0.01		E^+ ——	0.02		A_2^+ ——	0.03
$+58.82$	B_2^+ ——		$+58.81$	B_2^+ ——		$+58.71$	B_2^+ ——	
	E^- ——	0.06		E^- ——	0.07		E^- ——	0.54
	B_2^- ——	0.04		B_2^- ——	0.04		B_2^- ——	0.04
$+27.50$	A_2^- ——		$+27.48$	A_2^- ——		$+27.42$	A_2^- ——	
	E^+ ——	0.09		E^+ ——	0.09		B_1^+ ——	0.34
	B_1^+ ——	0.04		B_1^+ ——	0.03		A_1^+ ——	0.30
-1305.65	E^+ ——		-1305.63	A_1^+ ——		-1305.45	A_1^+ ——	

TABLE IX. $J=0$ energy levels obtained from a 5D calculation on the ASP1 surface using $j_{max}=10$ and different k_{max} values for the Wigner basis set attached to each monomer.

$k_{max}=10$			$k_{max}=8$			$k_{max}=6$		
	B_2^- ——	1.68		B_2^- ——	1.68		B_2^- ——	1.77
	E^- ——	1.05		E^- ——	1.04		E^- ——	0.75
+98.24	A_2^- ——		+98.25	A_2^- ——		+98.89	A_2^- ——	
	B_1^+ ——	10.41		B_1^+ ——	10.41		B_1^+ ——	10.45
	E^+ ——	7.98		E^+ ——	7.99		E^+ ——	8.51
+83.18	A_1^+ ——		+83.18	A_1^+ ——		+83.15	A_1^+ ——	
	A_2^+ ——	7.62		A_2^+ ——	7.61		A_2^+ ——	7.59
	E^+ ——	1.81		E^+ ——	1.80		E^+ ——	1.42
+72.88	B_2^+ ——		+72.89	B_2^+ ——		+73.34	B_2^+ ——	
	B_2^- ——	1.83		B_2^- ——	1.83		B_2^- ——	1.85
	E^- ——	1.07		E^- ——	1.05		E^- ——	0.35
+10.60	A_2^- ——		+10.61	A_2^- ——		+11.41	A_2^- ——	
	B_1^+ ——	2.47		B_1^+ ——	2.47		B_1^+ ——	2.47
	E^+ ——	1.82		E^+ ——	1.83		E^+ ——	2.47
−984.75	A_1^+ ——		−984.75	A_1^+ ——		−984.62	A_1^+ ——	

$$\mathbf{H}=-\frac{\hbar^2}{2\mu_{AB}}\frac{\partial^2}{\partial R^2}+\mathbf{H}_{rot}^{(A)}+\mathbf{H}_{rot}^{(B)}+\mathbf{V}(R,\underline{\Omega}^{(A)},\underline{\Omega}^{(B)})$$
$$+\frac{1}{2\mu_{AB}R^2}\{\mathbf{J}^2+\mathbf{j}^2-2\mathbf{j}\cdot\mathbf{J}\} \tag{4}$$

where

(1) R is the distance between the centers of mass of the two monomers A and B, and μ_{AB} their reduced mass,
(2) $\mathbf{H}_{rot}^{(\alpha)}$ and $\mathbf{j}_A$ are respectively the rotational Hamiltonian and angular momentum of monomer α,
(3) $\mathbf{j}=\mathbf{j}_A+\mathbf{j}_B$ is the coupled internal rotational angular momentum,
(4) $\mathbf{J}=\mathbf{j}+\ell$ the total angular momentum (ℓ is the angular momentum of the monomer centers of mass),
(5) and $\underline{\Omega}^{(\alpha)}\equiv(\varphi^{(\alpha)},\theta^{(\alpha)},\chi^{(\alpha)})$ represents the Euler angles defining the orientation of monomer α in the body fixed axes.

The parameters used in the calculations are given in Table I.

B. Spectral representations

The total spectral representation is written as the direct product

$$\mathscr{B}_{ang}\otimes\{|S_n\rangle,n=1,N_S\}$$

with the S's chosen as sine functions:

$$S_n(R)=\sqrt{\frac{2}{L}}\sin\frac{n\pi(R-R_{min})}{L}, \tag{5}$$

where $L=R_{max}-R_{min}$ is the box size. These provide a convenient basis set to describe the relative R motion confined to the interval $[R_{min},R_{max}]$.

In order to perform the calculations, several different angular bases $\mathscr{B}_{ang}$ are used, which are described below.

TABLE X. $J=0$ energy levels obtained from a 6D calculation using the Clementi and co-workers SCF/CI surface. Wigner basis sets corresponding to $j_{max}=11$ have been used on each monomer. Figures in parentheses correspond to the energy change in the level position associated to an increase in the basis set size from $j_{max}-1$ to its actual value of j_{max}.

	B_2^- ———	3.03 (+0.01)
	E^- ———	1.39 (+0.01)
+140.27 (+0.02)	A_2^- ———	
	A_2^+ ———	5.83 (+0.02)
	E^+ ———	2.16 (+0.04)
+136.62 (−0.08)	B_2^+ ———	
	E^+ ———	0.75 (−0.00)
	B_1^+ ———	0.75 (−0.00)
+129.13 (+0.03)	A_1^+ ———	
	B_1^- ———	1.38 (−0.00)
	E^- ———	0.40 (+0.05)
+114.57 (−0.06)	A_1^- ———	
	B_2^- ———	2.58 (−0.00)
	E^- ———	1.77 (+0.06)
+91.69 (−0.03)	A_2^- ———	
	B_1^+ ———	5.08 (−0.02)
	E^+ ———	3.00 (+0.04)
+77.31 (−0.07)	A_1^+ ———	
	A_2^+ ———	0.76 (−0.01)
	E^+ ———	0.23 (−0.05)
+69.81 (−0.02)	B_2^+ ———	
	B_2^- ———	0.89 (−0.00)
	E^- ———	0.52 (+0.01)
+16.72 (−0.02)	A_2^- ———	
	B_1^+ ———	0.76 (−0.00)
	E^+ ———	0.65 (−0.01)
−1060.08 (−0.12)	A_1^+ ———	

Downloaded¬27¬Jun¬2001¬to¬132.162.161.158.¬Redistribution¬subject¬to¬AIP¬license¬or¬copyright,¬see¬http://ojps.aip.org/jcpo/jcpcr.jsp

TABLE XI. Same as Table X for the RWK2 surface. A j_{max} value of 12 has been used for each monomer.

	A_1^- ———	0.21 (−0.03)
	B_1^- ———	0.11 (+0.03)
+168.41 (−0.07)	E^- ———	
	A_2^+ ———	0.32 (−0.00)
	E^+ ———	0.11 (+0.01)
+156.43 (−0.02)	B_2^+ ———	
	B_1^- ———	0.14 (−0.00)
	E^- ———	0.01 (−0.01)
+123.86 (−0.09)	A_1^- ———	
	E^- ———	0.14 (+0.01)
	B_2^- ———	0.09 (−0.00)
+106.23 (−0.05)	A_2^- ———	
	B_1^+ ———	0.48 (−0.00)
	E^+ ———	0.35 (−0.01)
+104.76 (−0.05)	A_1^+ ———	
	A_2^+ ———	0.06 (−0.02)
	B_2^+ ———	0.02 (−0.02)
+59.10 (−0.10)	E^+ ———	
	E^- ———	0.06 (−0.05)
	B_2^- ———	0.05 (+0.00)
+27.01 (−0.02)	A_2^- ———	
	E^+ ———	0.11 (+0.07)
	B_1^+ ———	0.04 (+0.00)
−1215.74 (−0.08)	A_1^+ ———	

TABLE XII. Same as Table X for the ASP1 surface. A j_{max} value of 10 has been used for each monomer.

	A_2^+ ———	13.52 (−0.01)
	E^+ ———	3.52 (+0.01)
+111.98 (−0.07)	B_2^+ ———	
	B_1^- ———	2.96 (−0.02)
	E^- ———	0.70 (−0.07)
+103.22 (+0.02)	A_1^- ———	
	E^- ———	2.86 (−0.07)
	B_2^- ———	1.86 (+0.02)
+91.39 (−0.01)	A_2^- ———	
	B_1^+ ———	8.98 (−0.03)
	E^+ ———	7.55 (−0.06)
+75.00 (−0.02)	A_1^+ ———	
	A_2^+ ———	4.94 (−0.03)
	E^+ ———	0.76 (+0.03)
+70.96 (−0.00)	B_2^+ ———	
	B_2^- ———	1.47 (−0.00)
	E^- ———	0.97 (−0.01)
+13.31 (−0.01)	A_2^- ———	
	B_1^+ ———	1.80 (−0.01)
	E^+ ———	1.80 (+0.01)
−923.74 (−0.13)	A_1^+ ———	

TABLE XIII. Same as Table X for the ASP2 surface. A j_{max} value of 10 has been used for each monomer.

	A_1^- ———	14.17 (−0.11)
	E^- ———	10.94 (−0.10)
+126.59 (+0.01)	B_1^- ———	
	B_1^+ ———	19.02 (−0.12)
	E^+ ———	9.78 (+0.03)
+121.70 (−0.08)	A_1^+ ———	
	B_2^- ———	17.25 (−0.10)
	E^- ———	3.11 (−0.01)
+117.25 (−0.01)	A_2^- ———	
	A_2^+ ———	15.59 (−0.09)
	E^+ ———	3.81 (−0.05)
+102.34 (−0.02)	B_2^+ ———	
	A_2^+ ———	2.47 (−0.02)
	E^+ ———	1.65 (+0.01)
+89.34 (−0.04)	B_2^+ ———	
	E^- ———	10.88 (−0.08)
	B_2^- ———	6.00 (−0.01)
+88.16 (−0.00)	A_2^- ———	
	A_1^- ———	7.07 (−0.02)
	B_1^- ———	7.07 (−0.03)
+85.93 (−0.03)	E^- ———	
	B_1^+ ———	10.99 (−0.02)
	E^+ ———	7.76 (−0.06)
+74.09 (+0.02)	A_1^+ ———	
	B_2^- ———	3.31 (−0.02)
	E^- ———	1.67 (−0.01)
+6.31 (−0.01)	A_2^- ———	
	B_1^+ ———	3.54 (−0.01)
	E^+ ———	3.24 (−0.03)
−981.65 (−0.10)	A_1^+ ———	

1. The uncoupled basis set $\mathscr{B}_{unc}$

This basis is defined as the direct product of Wigner bases $\{|j_\alpha, k_\alpha, \omega_\alpha\rangle\}$ on each monomer times a Wigner basis $\{|J, \Omega, M\rangle\}$ for the total angular momentum:

$$\mathscr{B}_{unc} = \{|j_A, k_A, \omega_A\rangle\} \otimes \{|j_B, k_B, \omega_B\rangle\} \otimes \{|J, \Omega, M\rangle\}.$$

It will only be used as an intermediate between the coupled representation and the grid (see Sec. II C).

Expressed in the uncoupled basis set $\mathscr{B}_{unc}$, the wave function displays many zero elements, depending on the J value. Figure 2 represents the case for $J=1$. In this figure, the ω_A and ω_B indices run between $-j_A$ and j_A, and $-j_B$ and j_B respectively. Due to the large j_A and j_B values used in order to reach convergence, the proportion of null elements is very high (up to 96% when $j_A = j_B = 13$ and $J=0$). This sparsity has been taken into account as only the non-zero elements were stored.

TABLE XIV. $J=1$ energy levels obtained from a 6D calculation using the Clementi and coworkers surface. Wigner basis sets corresponding to $j_{max}=10$ have been used on each monomer.

Energy	Symmetry	Value
	A_2^+ ———	2.58
	E^+ ———	1.71
+91.77	B_2^+ ———	
	B_1^+ ———	3.73
	E^+ ———	1.68
+83.36	A_1^+ ———	
	B_2^- ———	2.12
	E^- ———	0.72
+82.06	A_2^- ———	
	A_2^+ ———	2.12
	E^+ ———	0.72
+82.06	B_2^+ ———	
	A_1^- ———	5.10
	E^- ———	2.96
+77.39	B_1^- ———	
	B_2^- ———	0.77
	E^- ———	0.28
+68.92	A_2^- ———	
	B_2^- ———	0.72
	E^- ———	0.18
+19.70	A_2^- ———	
	A_2^+ ———	0.72
	E^+ ———	0.18
+19.70	B_2^+ ———	
	A_2^+ ———	0.89
	E^+ ———	0.51
+16.74	B_2^+ ———	
	B_1^+ ———	0.94
	E^+ ———	0.44
+12.60	A_1^+ ———	
	A_1^- ———	0.94
	E^- ———	0.44
+12.59	B_1^- ———	
	A_1^- ———	0.76
	E^- ———	0.66
−1059.57	B_1^- ———	

TABLE XV. Same as Table XIV for the ASP1 surface. A j_{max} value of 10 has been used for each monomer.

Energy	Symmetry	Value
	E^+ ———	2.86
	A_2^+ ———	1.86
+91.39	B_2^+ ———	
	A_1^- ———	5.42
	E^- ———	2.50
+83.07	B_1^- ———	
	B_1^+ ———	5.41
	E^+ ———	2.49
+83.07	A_1^+ ———	
	A_2^+ ———	5.21
	E^+ ———	0.01
+81.94	B_2^+ ———	
	B_2^- ———	5.21
	E^- ———	0.62
+81.94	A_2^- ———	
	A_1^- ———	8.98
	E^- ———	6.94
+75.00	B_1^- ———	
	B_2^- ———	4.93
	E^- ———	0.76
+70.96	A_2^- ———	
	B_2^- ———	1.35
	E^- ———	0.14
+18.13	A_2^- ———	
	A_2^+ ———	1.35
	E^+ ———	0.14
+18.13	B_2^+ ———	
	A_2^+ ———	1.47
	E^+ ———	0.97
+13.31	B_2^+ ———	
	B_1^+ ———	2.14
	E^+ ———	1.06
+11.61	A_1^+ ———	
	A_1^- ———	2.14
	E^- ———	1.06
+11.61	B_1^- ———	
	A_1^- ———	1.80
	E^- ———	1.79
−923.35	B_1^- ———	

2. The coupled basis set $\mathscr{B}_{cpl}$

In order to contract this angular basis, one can define the coupled basis set

$$\mathscr{B}_{cpl}=\{|j_A j_B k_A k_B ;j\Omega\rangle|J,\Omega,M\rangle\},$$

where

$$|j_A j_B k_A k_B ;j\Omega\rangle = \sum_{\omega_A+\omega_B=\Omega} \langle j_A j_B \omega_A \omega_B|j_A j_B j\Omega\rangle$$
$$\times |j_A,k_A,\omega_A\rangle|j_B,k_B,\omega_B\rangle, \qquad (6)$$

$$|j_A,k_A,\omega_A\rangle|j_B,k_B,\omega_B\rangle$$
$$= \sum_{j=|j_A-j_B|}^{j=j_A+j_B} \langle j_A j_B \omega_A \omega_B|j_A j_B j\Omega\rangle|j_A j_B k_A k_B ;j\Omega\rangle, \qquad (7)$$

$\langle j_A j_B \omega_A \omega_B|j_A j_B j\Omega\rangle$ being a Clebsch–Gordan coefficient.

TABLE XVI. Same as Table XIV for the ASP2 surface. A j_{max} value of 10 has been used for each monomer.

	A_2^+ ———	6.00
	E^+ ———	1.47
+88.15	B_2^+ ———	
	A_1^+ ———	7.07
	B_1^+ ———	7.06
+85.93	E^+ ———	
	A_1^+ ———	6.65
	B_1^+ ———	0.60
+82.92	E^- ———	
	B_1^+ ———	6.65
	A_1^+ ———	0.61
+82.90	E^+ ———	
	A_1^- ———	10.97
	E^- ———	7.76
+74.09	B_1^- ———	
	B_2^- ———	3.23
	E^- ———	0.92
+12.86	A_2^- ———	
	A_2^+ ———	3.23
	E^+ ———	0.92
+12.86	B_2^+ ———	
	B_1^+ ———	4.01
	E^+ ———	2.36
+9.46	A_1^+ ———	
	A_1^- ———	4.01
	E^- ———	2.36
+9.46	B_1^- ———	
	A_2^+ ———	3.31
	E^+ ———	1.67
+6.31	B_2^+ ———	
	A_1^- ———	3.54
	E^- ———	3.24
−981.25	B_1^- ———	

This representation is used to compute the $\mathbf{H}_{rot}^{(A)}$, $\mathbf{H}_{rot}^{(B)}$, and centrifugal+Coriolis terms as will be shown later on.

3. The symmetry adapted bases $\mathscr{B}_{sym}^{(\Gamma)}$

The G_{16} permutation-inversion symmetry of the (H$_2$O)$_2$ complex allows us to subdivide the angular basis set into 10 symmetry adapted bases, corresponding to the different irreducible representations (Irrep) Γ's. The way to construct symmetry adapted vectors $|j_A j_B k_A k_B ; j\Omega, \Gamma\rangle$ from the coupled basis vectors,

$$|j_A j_B k_A k_B ; j\Omega, \Gamma\rangle$$

$$= c_1^{(\Gamma)} |j_A j_B k_A k_B ; j\Omega\rangle + c_2^{(\Gamma)} |j_B j_A k_B k_A ; j\bar{\Omega}\rangle$$

$$+ c_3^{(\Gamma)} |j_A j_B \bar{k}_A \bar{k}_B ; j\bar{\Omega}\rangle + c_4^{(\Gamma)} |j_B j_A \bar{k}_B \bar{k}_A ; j\Omega\rangle, \qquad (8)$$

where $\bar{k} \equiv -k$, is given in Table II.

In the following, we will use $\{|\nu\rangle_\Gamma, \nu = 1, N_\Gamma\}$ as a short-hand notation for the elements of the symmetry adapted basis corresponding to the Irrep Γ, and $\{|i\rangle_\omega, i = 1, N_\omega\}$ for the elements of the coupled basis set.

C. Grid representation

The different spectral representations defined just above allows one to easily compute the effect of the various parts of the Hamiltonian operator, except for the potential. The complete scheme will be presented in the next subsection. Now we discuss how the potential term is handled.

The method to evaluate the potential term consists in using a general pseudospectral method as defined by Friesner[27] for the case of electronic structure calculations. This method resorts to an intermediate grid representation, tantamount to making use of a quadrature rule in order to compute the matrix elements in the spectral representation. The potential function depends on the 6 coordinates $\{\theta^{(A)}, \chi^{(A)}, \theta^{(B)}, \chi^{(B)}, \varphi = \varphi^{(A)} - \varphi^{(B)}, R\}$, where $(\varphi^{(A)}, \theta^{(A)}, \chi^{(A)})$ represents the three Euler angles orienting monomer α in the BF frame. The grid representation corresponds to the set of values $\{\Psi_{\alpha q \beta s g p}\}$ taken by the wave function Ψ on the 6D grid $\{\theta_\alpha^{(A)} \times \chi_q^{(A)} \times \theta_\beta^{(B)} \times \chi_s^{(B)} \times \varphi_g \times R_p\}$.

The most convenient basis set to start from in order to transform to the grid representation is the uncoupled one $\mathscr{B}_{ang} \otimes \{|S_n\rangle, n = 1, N_S\}$. That is, starting from a wave function expressed as

$$|\Psi^{JM}\rangle = \sum_{j_A, k_A, j_B, k_B, \omega_A + \omega_B = \Omega, n} \Psi_{j_A k_A \omega_A j_b k_B \omega_B n}^{JM}$$

$$\times |j_A, k_A, \omega_A\rangle |j_B, k_B, \omega_B\rangle |J, \Omega, M\rangle |S_n\rangle, \qquad (9)$$

one wants to compute its amplitudes $\{\Psi_{\alpha q \beta s g n}^{JM}\}$ on the grid. This spectral-to-grid transform is performed in several successive steps.

The first step consists in switching from the radial basis set $\{|S_n\rangle, n = 1, N_S\}$ to a grid $\{R_p = R_{min} + p\Delta R\}$ by means of the orthogonal collocation matrix[73]

$$U_{pn}^{(R)} = \sqrt{\frac{2}{N_R + 1}} \sin \frac{n\pi p}{N_R + 1}. \qquad (10)$$

It should be recalled here that we are using a number N_R of grid points larger than the number N_S of sine functions. This matrix allows one to define the intermediate representation $\{\Psi_{j_A k_A \omega_A j_b k_B \omega_B p}^{JM}\}$ by means of the transformation

$$\Psi_{j_A k_A \omega_A j_b k_B \omega_B p}^{JM} = \sum_n U_{pn}^{(R)} \Psi_{j_A k_A \omega_A j_b k_B \omega_B n}^{JM}. \qquad (11)$$

The inverse (grid to spectral) transform is performed by means of the inverse operation

$$\Psi_{j_A k_A \omega_A j_b k_B \omega_B n}^{JM} = \sum_n (U_{np}^{(R)})^+ \Psi_{j_A k_A \omega_A j_b k_B \omega_B p}^{JM}. \qquad (12)$$

The second step deals with the angular to Euler grid transformation. One of us[32] recently showed how one can
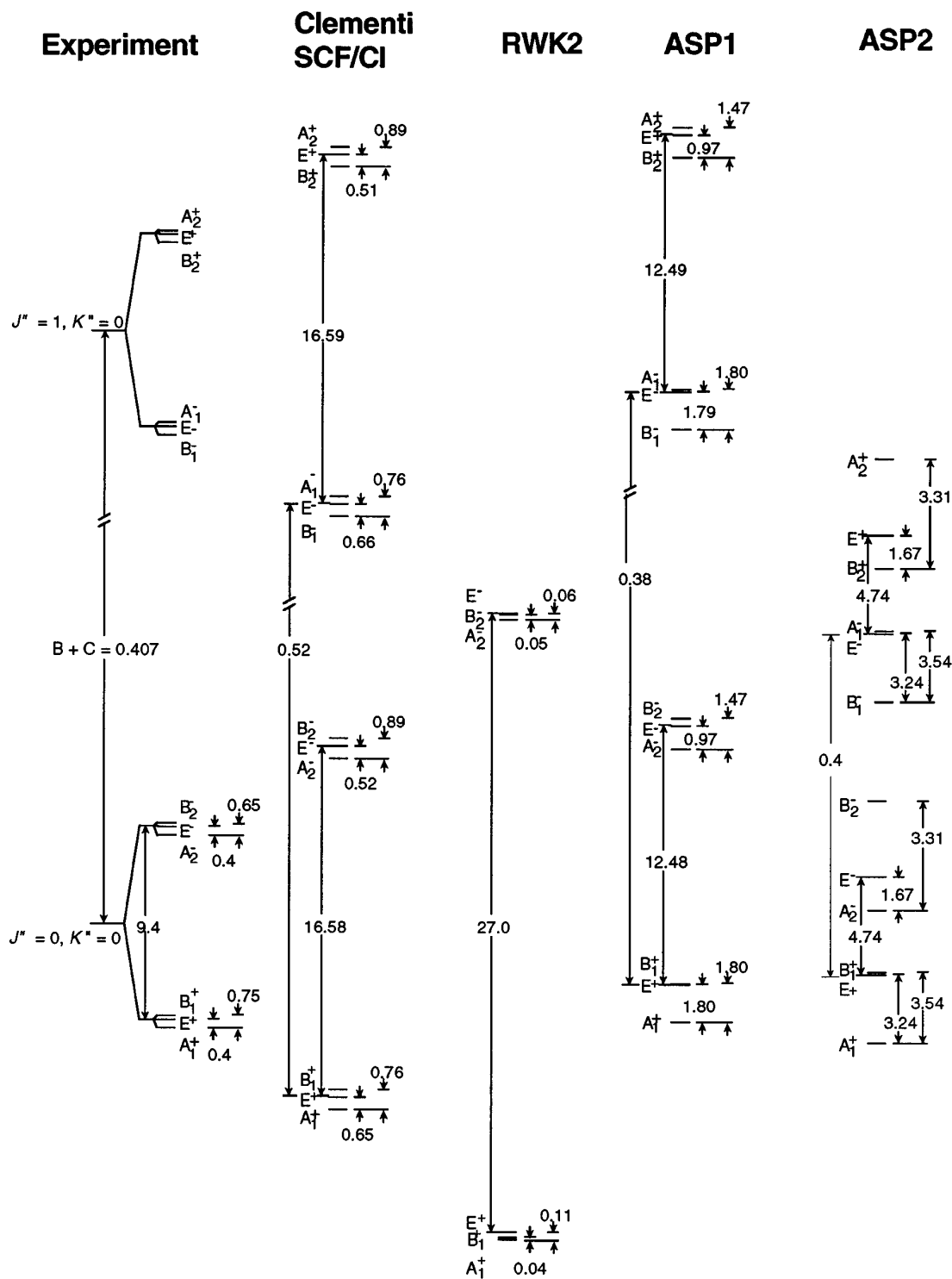
FIG. 3. Energy level diagrams obtained from experiments, the Clementi SCF/CI, the RWK,2 the ASP1 and ASP2 surfaces.

transform from a Wigner basis set $\{\mathscr{D}^j_{mk}(\varphi,\theta,\chi)\}$ to a 3D grid $\{\varphi_g \times \theta_\alpha \times \chi_q)\}$ associated with the Euler angles (the reader is referred to this paper for more details on the method which will be briefly recalled below). For a wave function specified by its components on a Wigner basis set

$$\psi = \sum_{jkm} \psi_{jkm} \mathscr{D}^j_{mk}, \tag{13}$$

the method first performs a Legendre transform

$$\psi_{\alpha km} = \sum_j R^{(m,k)}_{\alpha j} \psi_{jkm}, \tag{14}$$

where $R^{(m,k)}_{\alpha j}$ is the orthogonal matrix

Interchange Tunneling Splitting (J=0)

(a)   (cm-1)

Acceptor Tunneling Splitting (J=0)

(b)   (cm-1)
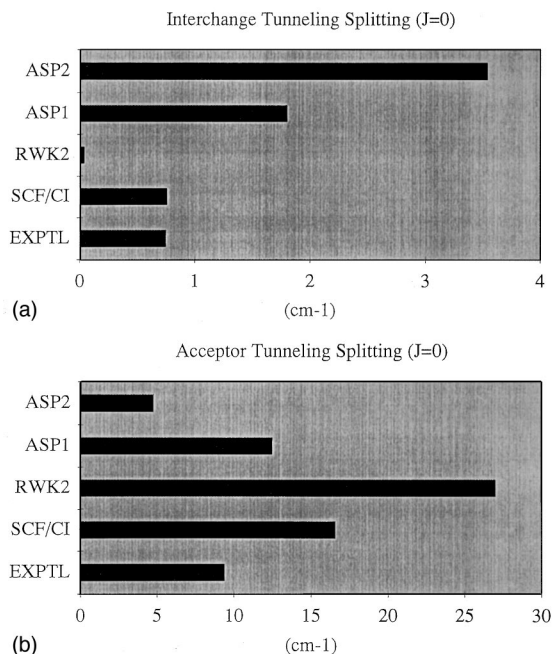
FIG. 4. $J=0$ tunneling splittings obtained from experiments, the Clementi SCF/CI, the RWK2, the ASP1 and ASP2 surfaces.

Interchange Tunneling Splitting (J=1,K=0)

(a)   cm-1

Acceptor Tunneling Splitting (J=1,K=0)

(b)   cm-1

FIG. 5. Same as Fig. 4 for total $J=1$.

$$R_{\alpha j}^{(m,k)} = \sqrt{\frac{2j+1}{2}} d_{mk}^{j}(\cos\theta_\alpha)\sqrt{\omega_\alpha}, \tag{15}$$

$\cos\theta_\alpha$ and ω_α being respectively the abscissae and weights of a N_θ points Gauss–Legendre quadrature, followed by a double inverse Fourier transform over φ and χ:

$$\{\psi_{\alpha qg}\} = \mathscr{F}_{\varphi\chi}^{-1}\{\psi_{\alpha km}\}. \tag{16}$$

The global inverse transform (grid→spectral) is performed by first direct Fourier transforming

$$\{\psi_{\alpha km}\} = \mathscr{F}_{\varphi\chi}\{\psi_{\alpha qg}\}, \tag{17}$$

followed by the reverse Legendre transform

$$\psi_{jkm} = \sum_\alpha R_{\alpha j}^{(m,k)}\psi_{\alpha km}. \tag{18}$$

This scheme has to be adapted to the case considered here, as the potential **V** depends only on the $\varphi = \varphi^B - \varphi^A$ angle, and not on $\Phi = \varphi^B + \varphi^A$. Consequently, the $\Omega = \omega_B + \omega_A$ index is a good quantum number with respect to **V**, as can be seen from the equivalence

$$e^{i\omega_A\varphi^A}e^{i\omega_B\varphi^B} = e^{1/2(\Omega\Phi + \omega\varphi)}, \tag{19}$$

where $\omega = \omega_B - \omega_A$. It has been shown by Halberstadt[74] that due to symmetry, the integration over φ can be made independent of the Φ variable, and running from 0 to 2π. It results that the following integral

$$\frac{1}{4\pi^2}\int_0^{2\pi} d\varphi_A \int_0^{2\pi} d\varphi_B e^{-i(\omega_A\varphi^A + \omega_B\varphi^B)}$$

$$\times V(\varphi^B - \varphi^A)e^{i(\omega_A'\varphi^A + \omega_B'\varphi^B)} \tag{20}$$

can be recast into the equivalent one

$$\delta_{\Omega\Omega'}\frac{1}{2\pi}\int_0^{2\pi} d\varphi\, e^{-1/2\omega\varphi}V(\varphi)e^{1/2\,\omega'\varphi}. \tag{21}$$

The transformation from the angular spectral representation to the five-dimensional grid can thus be realized by the following successive operations, performed for every value $\Omega = \omega_B + \omega_A$ compatible with the J value:

(i) transform to the $\{\theta_\alpha^A \times \theta_\beta^B\}$ grid

$$\Psi_{\alpha k_A\beta k_B\omega p}^{JM\Omega}$$

$$= \sum_{j_A j_B, \omega_B + \omega_A = \Omega} R_{\alpha j_A}^{(\omega_A, k_A)} R_{\beta j_B}^{(\omega_B, k_B)}\Psi_{j_A k_A\omega_A j_B k_B\omega_B p}^{JM}, \tag{22}$$

(ii) transform to the $\{\chi_q^{(A)} \times \chi_s^{(B)} \times \phi_g\}$ grid by a 3D inverse Fourier transform

$$\{\Psi_{\alpha q\beta sgp}^{JM\Omega}\} = \mathscr{F}_{\chi^A\chi^B\varphi}^{-1}\{\Psi_{\alpha k_A\beta k_B\omega p}^{JM\Omega}\}. \tag{23}$$

Going back to the $\{|j_A, k_A, \omega_A\rangle|j_B, k_B, \omega_B\rangle\}$ representation is realized by applying the inverse transforms in reverse order, i.e., (ii) then (i).

D. The split Hamiltonian formulation

This is basically the same scheme as the one used previously by one of us (C.L.) for the Ar–H$_2$O complex,[32] the differences coming only from the number of terms of the Hamiltonian operator. It consists in repetitively applying **H** on the wave function expressed in the $\mathscr{B}_{sym}^{(\Gamma)}\otimes\{|S_n\rangle\}$ basis set
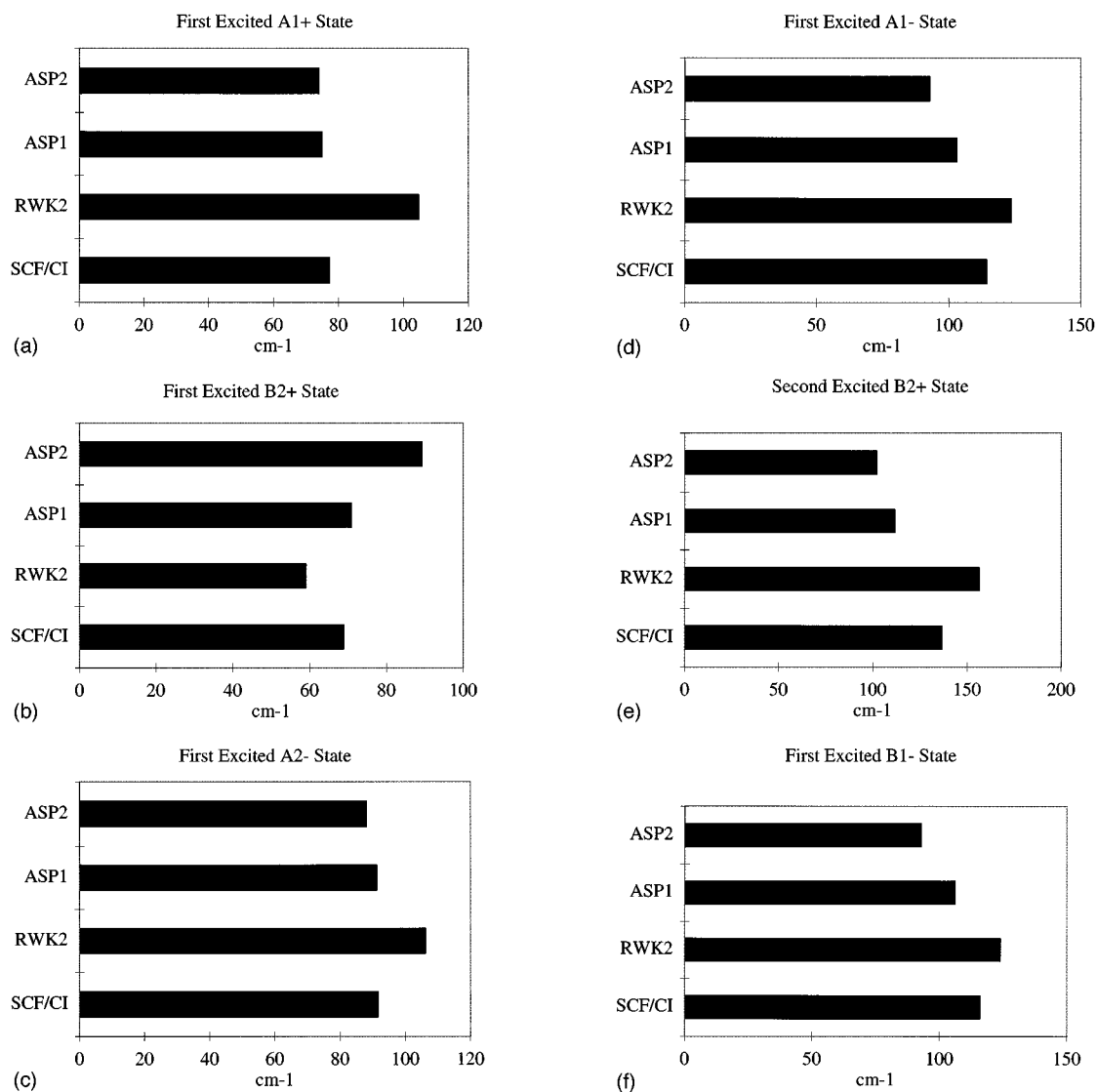
FIG. 6. Comparison of low-lying intermolecular vibrations as obtained from an exact 6D calculation for the different potential energy surfaces: (a) first excited A_1^+ state; (b) first excited B_2^+ state; (c) first excited A_2^- state; (d) first excited A_1^- state; (e) second excited B_2^+ state; (f) first excited A_1^- state.
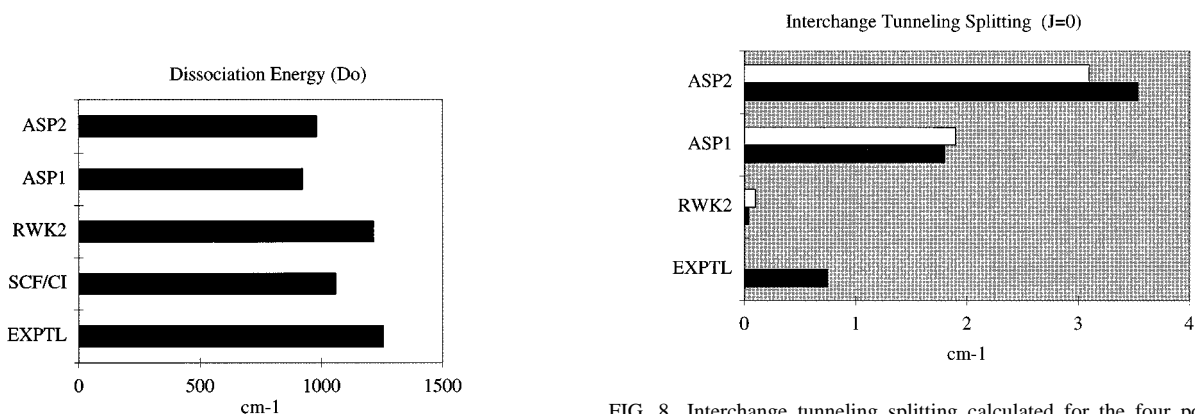
FIG. 7. Same as Fig. 6 for the dissociation energy D_0.

FIG. 8. Interchange tunneling splitting calculated for the four potentials with the exact SWPS (black bars) or approximate RAA (white bars) method, as compared to the experimental value.

Acceptor Tunneling Splitting (J=0)
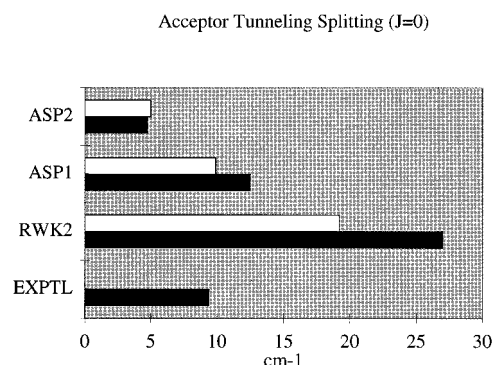
FIG. 9. Same as Fig. 8 for the acceptor tunneling splitting.

O-O Torsion (v12)

(a)

Acceptor Bend (v8)

(b)

Acceptor Rotation (v11)

(c)
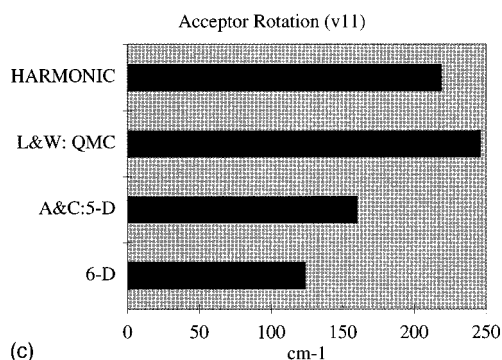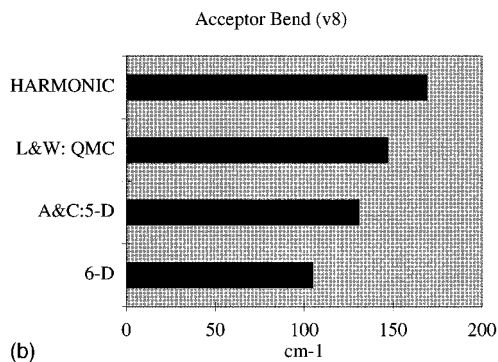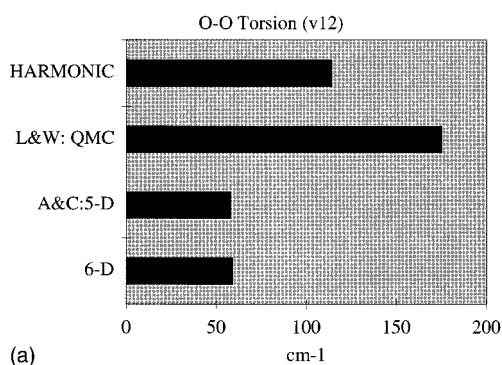
FIG. 10. Comparison of results, using the RWK2 surface, as obtained from the harmonic approximation, the Lewerenz and Watts (Refs. 62) QMC calculations, the Althorpe and Clary (Ref. 66,67) RAA calculations, and our 6D SWPS calculations (a) O–O torsion frequency ν_{12}; (b) acceptor bend frequency ν_8; (c) acceptor rotation ν_{11}.

Interchange Tunneling Splitting

(a)

Acceptor Tunneling Splitting

(b)

Dissociation Energy (Do)

(c)
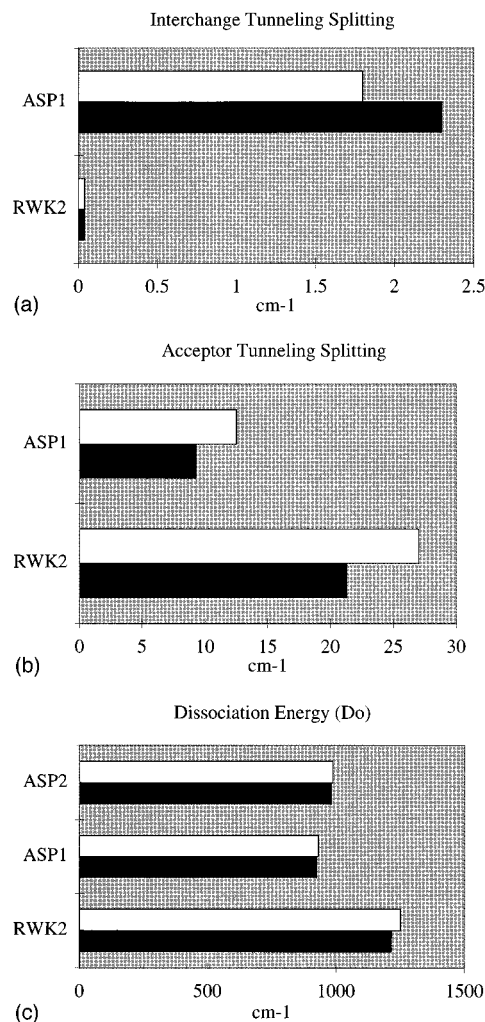
FIG. 11. Comparison of results, using the RWK2 surface, as obtained from DQMC (black bars) or SWPS (white bars) calculations: (a) interchange tunneling splitting; (b) acceptor tunneling splitting; (c) dissociation energy D_0.

$$|\Psi^{JM\Gamma}\rangle = \sum_{\nu\Omega n} \Psi^{JM\Gamma}_{\nu\Omega n} |\nu,\Omega\rangle |J\Omega M\rangle |S_n\rangle \qquad (24)$$

in order to propagate the Lanczos scheme. The choice of the symmetry adapted basis results from the fact that it constitutes the most compact basis for expressing the Lanczos vectors $\{|u_n\rangle\}$. We now briefly recall the Lanczos algorithm, and then discuss the different terms into which the Hamiltonian was split, as well as their associated representations.

Starting from some initial vector $|u_0\rangle$, the Lanczos algorithm[36] recursively generates the Krylov space $\{|u_n\rangle n = 0, N_L\}$

$$\beta_{n+1}|u_{n+1}\rangle = (\mathbf{H} - \alpha_n)|u_n\rangle - \beta_n|u_{n-1}\rangle, \qquad (25)$$

where $\alpha_n = \langle u_n|\mathbf{H}|u_n\rangle$ and $\beta_{n+1} = \langle u_{n+1}|\mathbf{H}|u_n\rangle$ are respectively the diagonal and off-diagonal terms of $\mathbf{H}$ in this new basis set.

In order to perform the recursions, $\mathbf{H}$ as given by Eq. (4) has been split into 4 terms, namely

$$\mathbf{H} = \mathbf{T}_R + \mathbf{H}_{AB} + \mathbf{H}_{cc} + \mathbf{V}, \qquad (26)$$

where each term has been handled as shown below.

1. Radial kinetic energy T_R

This term, $\mathbf{T}_R = -\hbar^2/2\mu_{AB}\,\partial^2/\partial R^2$, is diagonal in the initial representation (Eq. 24), resulting in the effect

$$\mathbf{T}_R|\Psi^{JM\Gamma}\rangle = \sum_{\nu\Omega n} \frac{(n\pi\hbar)^2}{2\mu_{AB}} \Psi_{\nu\Omega n}^{JM\Gamma}|\nu,\Omega\rangle|J\Omega M\rangle|S_n\rangle. \quad (27)$$

2. Monomer rotational terms $H_{AB}=H_A+H_B$

The rotational kinetic energy term $\mathbf{H}_\alpha$ displays analytic expressions in a Wigner basis set $\{|jk\omega\rangle\}$ given by

$$\mathbf{H}_\alpha|jk\omega\rangle = \{\tfrac{1}{2}(B_x+B_y)(j(j+1)-k^2)+B_z k^2\}|jk\omega\rangle$$
$$+ \tfrac{1}{4}(B_x-B_y)F_{jk}^+|jk+2\omega\rangle$$
$$+ \tfrac{1}{4}(B_x-B_y)F_{jk}^-|jk-2\omega\rangle, \quad (28)$$

where $F_{jk}^\pm = [j(j\pm1)-k(k\pm1)]^{1/2}[j(j\pm1)-(k\pm1)(k\pm2)]^{1/2}$. In order to exploit the above relations, one has to switch to the coupled basis set $\mathcal{B}_{\mathrm{cpl}}$

$$|\Psi^{JM\Gamma}\rangle = \sum_{j_A k_A j_B k_B j\Omega n} \Psi_{j_A k_A j_B k_B j\Omega n}^{JM\Gamma}|j_A j_B k_A k_B;j\Omega\rangle$$
$$\times|J,\Omega,M\rangle|S_n\rangle. \quad (29)$$

As Eq. (28) only involves changes in the k index, the $\mathbf{H}_\alpha$ terms can be directly applied in this representation.

3. Coriolis and centrifugal term H_{CC}

This term, $\mathbf{H}_{CC}=1/2\mu_{AB}R^2\{\mathbf{J}^2+\mathbf{j}^2-2\mathbf{j}\cdot\mathbf{J}\}$ also displays simple analytic expressions in the coupled angular basis set

$$\mathbf{H}_{CC}|j\Omega\rangle|J,\Omega,M\rangle$$
$$= [J(J+1)+j(j+1)-2\Omega^2]|j\Omega\rangle|J,\Omega,M\rangle$$
$$+ C_{J\Omega}^+ C_{j\ \Omega}^+|j\Omega+1\rangle|J,\Omega+1,M\rangle$$
$$+ C_{J\Omega}^- C_{j\Omega}^-|j\Omega-1\rangle|J,\Omega-1,M\rangle, \quad (30)$$

where $C_{j\Omega}^\pm = [j(j\pm1)-\Omega(\Omega\pm1)]^{1/2}$. The $1/2\mu_{AB}R^2$ factor in front of $\mathbf{H}_{CC}$ is handled by switching to the $\{R_p\}$ grid, where it is diagonal, by means of Eq. (11)

$$\{\Psi_{j_A k_A j_B k_B j\Omega n}^{JM\Gamma}\} \rightarrow \{\Psi_{j_A k_A j_B k_B j\Omega p}^{JM\Gamma}\} \quad (31)$$

4. Potential term V

As discussed before, this last term is diagonal in the 6D grid times the total angular momentum representation $\{\theta_\alpha^{(A)}\times\chi_q^{(A)}\times\theta_\beta^{(B)}\times\chi_s^{(B)}\times\Phi_g\times R_p\}\otimes\{|J,\Omega,M\rangle\}$, which can be reached, as discussed in Sec. II C, by means of Eqs. (22–23)

$$\{\Psi_{j_A k_A j_B k_B j\Omega p}^{JM\Gamma}\} \rightarrow \{\Psi_{\alpha q\beta s g p}^{JM\Gamma\Omega}\cdot\} \quad (32)$$

Once a term of $\mathbf{H}$ has been applied in its own representation, the result is transformed back to the symmetrized times the sine functions basis set $\mathcal{B}_{\mathrm{sym}}\otimes\{|S_n\rangle\}$ in which the Lanczos vectors are expressed.

III. ANGULAR BASIS CONVERGENCE TESTS

In this section, we study the size of the angular basis sets required in order to converge the calculations. This is realized by computing the energy levels at a fixed relative separation R_* for increasing angular basis sizes until convergence is reached. We used for R_* the value ($R_* = 5.6242$ a.u.) close to the equilibrium geometry of the dimer. As will be shown in the next section, such fixed R calculations are much faster than full 6D ones including the R coordinate. Four different water dimer potential energy surfaces are successively studied, namely the Clementi and co-workers's,[70] the RWK2[63] and the ASP1 and ASP2[65] surfaces. These convergence tests are then used in the next section. In the first series of calculations presented, no restriction has been applied to the uncoupled angular basis set, except for the maximum j value $j_{\max}$ allowed for each monomer. The $k_{\max}=j_{\max}$ constraint will then be relaxed in subsequent calculations.

A. Unrestricted angular basis

In this case, the angular basis set for each monomer reads as

$$\{|j_\alpha,k_\alpha,\omega_\alpha\rangle,-j_\alpha\leq\omega_\alpha\leq j_\alpha;-j_\alpha\leq k_\alpha\leq j_\alpha;0\leq j_\alpha\leq j_{\max}\}.$$

The convergence tests consist of increasing this $j_{\max}$ value. The angular basis set is therefore specified by a single parameter, $j_{\max}$. The grid representation of the angular wave function involves other parameters, namely the numbers of grid points associated with each of the five Euler angles. We found by experimentation that using 2–3 more points than the number of functions associated with an angle ensures convergence of the results with respect to the basis definition. For example, the θ grid dimension was set to $N_\theta=j_{\max}+3$, while for the χ and φ grids $N_\chi=N_\varphi \geq (2j_{\max}+1)+2$. This latter inequality reflects the fact that the χ and φ angles were handled by fast Fourier transform (FFT) routines which restrict the allowed dimensions.

As described so far, this scheme would generate huge grid sizes, of dimension of the order of $(j_{\max}+3)^2[(2j_{\max}+1)+2]^3$. The vast majority of these grid points are associated with geometries corresponding to very high potential energies, close to or above the dissociation threshold ($V=0$). At these points, the wave function has to be negligible for bound states localized near the bottom of the well (located at circa -1800 cm^{-1}). For our present concerns, one can thus safely ignore these points and set the corresponding amplitudes to zero when transforming to the grid representation. In practice, we have used an energy threshold of $V_{\mathrm{thres}}=-300$ cm^{-1} for the potential, restricting the grid definition to the points located below this threshold. The results for all four potential energy surfaces are given in Tables III–VI, and are discussed now.

These tables are organized in such a way as to display the acceptor and interchange tunneling splittings, even though those quantities should be computed from a 6D calculation (see Sec. IV). Only the levels converged to within

0.01 cm^{-1} with respect to the Lanczos scheme have been reported.

In each table, the different columns display respectively the ground (A_1^+) energy, the relative position of each acceptor tunneling manifold band, the associated symmetry sublevels, and finally their relative energies with respect to the band origin. The figures in parentheses provide an estimate of the convergence with respect to the angular basis set, as specified by j_{max}. They correspond to the energy change in the level position associated to an increase in the basis set size from $j_{max}-1$ to its actual value of j_{max}. It results from these tables that large j_{max} values have to be used (≥ 10), in order to converge the energy levels within a few hundredths of a wave number. It should be noticed that a particularly high value, $j_{max}=13$, had to be used for the RWK2 surface in order to converge the symmetry pattern for each acceptor tunneling manifold.

B. Restricted angular basis

In order to test the actual angular basis required for convergence of the splittings, we have relaxed the $k_{max}=j_{max}$ constraint in a second series of calculations. More specifically, keeping j_{max} at the values precedently obtained, we have reduced the maximum value k_{max} allowed for the k index. The results, displayed in Tables VII–IX for three of the surfaces, show the following trends:

(i)   the positions of the degenerate levels ($E^{\pm}$) start to significantly change for $k_{max} \leq j_{max}-2$,
(ii) the acceptor tunneling splittings are correctly described down to $k_{max} \simeq j_{max}-4$,
(iii) for the interchange tunneling splittings, the k_{max} values can safely be further reduced to $j_{max}-5$ without noticeable relative changes.

IV. RESULTS

A. Assessing the model potentials

The results of the fully converged 6D calculations of the water dimer VRT states are presented in Tables X–XVI. (The expensive $J=1$ calculations were not performed for the RWK2 surface as the $J=0$ results are already in poor agreement with experiments.)

Energy level diagrams showing the acceptor and interchange tunneling splittings in the $J=0,1$ and $K=0,1$ states of the vibrational ground state corresponding to each of the four potentials examined in this work are given in Fig. 3, together with the experimental energy levels deduced from microwave and far-IR spectroscopy. *It is immediately clear upon inspecting these diagrams that none of the potential surfaces examined in this work can describe the eigenstates of the water dimer at even a qualitatively correct level of detail*. To illustrate the nature of the discrepancies in detail, bar graphs of the acceptor and interchange tunneling splittings and rotational constants $(B+C)/2$ calculated by the SWPS method for each of the four potentials are presented along with the experimental results in Figs. 4 and 5.

The Clementi and co-workers self-consistent field/

configuration interaction (SCF/CI) potential does very well in reproducing the experimental interchange splitting, but badly overestimates the effects of acceptor tunneling. The RWK2 potential, widely regarded as the best effective water dimer surface, drastically underestimates (by an order of magnitude) the interchange splitting and overestimates the acceptor splitting by a factor of 3. It is also the most anisotropic surface, requiring the largest angular basis, as described in the previous section. The ASP1 surface badly overestimates the interchange splitting and is somewhat high for the acceptor tunneling, whereas ASP2 exaggerates the interchange splitting by a factor of 5 and underestimates the acceptor splitting. Interestingly, the only difference between these two highly detailed distributed multipole potential models[65] with Tang–Toennies damping functions is in the treatment of dispersion, with ASP2 incorporating the extensive results of Rijks and Wormer,[75,76] while ASP1 uses the perturbation theory results of Szczesniac *et al.*[77] This illustrates the extreme sensitivity of the VRT dynamics to the details of the dispersion interactions, which is perhaps surprising since the intermolecular attraction is dominated by electrostatics in all of these models.

On the other hand, the *structure* of the dimer expressed in the rotational constants is quite well represented by all four potentials. This illustrates an important point: *The structure of a hydrogen bonded complex does not provide a sensitive probe of the intermolecular potential; it is therefore of limited use by itself for characterizing intermolecular forces, being a necessary but not sufficient constraint.* The tunneling splittings and (as we shall see) intermolecular vibrations, however, provide an *exacting* measure of the potential energy, and can therefore serve as a direct route for their experimental determination. This has been shown previously for the simpler cases of Ar–HCl,[3] Ar–H$_2$O,[12] and Ar–NH$_3$.[13] Not surprisingly, the four water dimer potentials examined here differ widely in the representation of the intermolecular vibrations, as shown in Fig. 6, and differ considerably in the values they produce for the ground state (vibrationally averaged) dissociation energy (Fig. 7), as well as for the ground state tunneling splittings.

B. VRT Dynamics: 5D vs 6D treatments

Due to the difficulties inherent in carrying out a completely rigorous treatment of the intermolecular dynamics occurring in weakly bound complexes, usually involving several fully coupled degrees of freedom, it has been customary to employ various approximate methods for this purpose. For those cases which have been examined in detail, viz. Ar–H$_2$O,[12] and Ar–NH$_3$,[13] it has been shown that the exclusion of the radial motion from the explicitly coupled dynamics leads to serious errors when angular-radial coupling in the potential mixes stretching and bending states. It is therefore important to explore the consequences of adiabatically separating, or simply fixing R in calculations of the water dimer VRT dynamics.

The most common of these is the reversed adiabatic ap-

proximation (RAA), in which the center of mass distance (R) is held fixed during a fully coupled calculation with the Euler angles, and the calculation repeated at a series of R values. The resulting one-dimensional radial Schrödinger equation is then solved for each angular eigenstate. For the water dimer, this approach involves explicitly solving a five-dimensional angular Hamiltonian, which can be done efficiently in a basis of Wigner functions. Althorpe and Clary have published two 5D treatments of the VRT dynamics in the water dimer, one employing a direct diagonalization at three values of R and subsequent computation of the radial eigenvalues for each symmetry[66] and the other a novel DVR approach[67] at a fixed value of R.

In Figs. 8 and 9, we compare our rigorous SWPS results with the RAA calculations of Althorpe and Clary.[66] In these graphs, the exact 6D calculations are given in black, while the white bars represent the results of approximate 6D (RAA) calculations (see below). From these figures, we can see that the two calculations give similar results for the $J=0$ interchange splittings, but widely different values for the acceptor splittings. Our energy levels were obtained with considerably larger basis sets (up to $j=13$ on both monomers and including all relevant k values) and yielding fully converged (to 0.01 cm^{-1}) energies, and differ significantly from theirs. In the RAA calculations, the basis was truncated at $j_{max}=8$ and $k_{max}=4$ for both monomers (being of dimension 3300 for nondegenerate representations and about four times larger for the E states) and incorporated the coupled states approximation (i.e., treating K as a conserved quantity). Moreover, memory restrictions limited their calculations to $K=0$ and $J=0$. Energy level convergence to within 0.5–1.0 cm^{-1} was claimed in their study. Comparison between their direct diagonalization FBR method and their DVR approach implied a combined error from truncation of the potential expansion and convergence not exceeding 2 cm^{-1} for the first two levels of each symmetry and less than 0.2 for the ground state tunneling splittings. Hence, at least part of the difference between our SWPS results and the RAA calculations is in the level of convergence, but the principal difference lies again in the fact that the R motion must be rigorously included in the dynamics if truly quantitative results are to be obtained.

C. VRT dynamics: WDVR vs quantum Monte Carlo methods

Watts and co-workers[14,15,62] have pioneered the use of diffusion quantum Monte Carlo methodology for calculating properties of hydrogen bonded clusters,[14,15] with extensive applications to the water dimer. This approach permitted a fully coupled treatment of the VRT dynamics, ideally yielding exact (for a given potential) results for the ground state. Calculations of the properties of excited states are notoriously difficult to carry out, however, due to the requirement for accurate knowledge of the nodal surfaces of the excited state wave function. Nevertheless, Watts and co-workers have published calculations for both the ground state and for

excited vibrational states (both intra- and inter-molecular) employing the QMC method. Recently, Gregory and Clary[17] have achieved much higher accuracy for ground state properties of the water dimer with a combination of correlated sampling techniques and the rigid body diffusion quantum Monte Carlo (RBDQMC) approach developed by Buch.[18] By employing exact nodal constraints derived from the molecular symmetry group, they were able to efficiently compute the tunneling splittings in the ground vibrational state of the dimer. In Figs. 10 and 11, we compare our SWPS results against those obtained with QMC methods for both ground state properties and for several excited intermolecular vibrational states, using the RWK2 potential surface. It is immediately apparent that the excited state QMC results[62] are very inaccurate, again due to the severe problems associated with rigorously specifying the nodal constraints. The potentially more accurate RBDQMC results for the ground state tunneling splittings are in good agreement with the SWPS results.

D. The intermolecular vibrations

Values calculated with the SWPS method for the lowest (below 150 cm^{-1}) excited intermolecular vibrations are presented in Fig. 9. As the eigenvectors were not computed in this work, we are not currently able to specify the nature of these vibrations. Lewerenz and Watts[62] did so for a few low-lying vibrations in their QMC treatment (see Fig. 11), but as we have discussed above, their results are highly inaccurate due to the problems inherent in specifying the nodal surfaces for these excited eigenstates. It is clear from their work, however, that the intermolecular vibrations of the water dimer cannot be described as normal modes, and generally involve all six large amplitude coordinates. In Fig. 11, we compare the normal mode frequencies calculated with the RWK2 potential by Coker and Watts,[15] and a set of harmonic frequencies from a recent *ab initio* calculation.[69] We see that these disagree by as much as a factor of 2 for some low-lying excited states.

V. DISCUSSION

The rigorous 6D SWPS results presented here for the water dimer VRT dynamics permit a number of general conclusions to be drawn regarding previous work and future directions. First, while the approximate 5D methods cannot be used for quantitative comparison of potential surfaces, they may be useful in the initial stages of an IPS fit to spectroscopic data. The exciting new advances in DQMC methodology may ultimately be combined with SWPS for this purpose, as these are cheaper and may allow non-pairwise contributions to the IPS of large clusters to be added in a systematic way[78] as recently shown by Gregory and Clary.[17,64,71] Specifically, they showed that by adding the iterated many-body induction and three-body dispersion interactions to the ASP pair potential, they were able to reproduce the *structures* of the water trimer, tetramer, pentamer

and hexamer recently determined by far-IR laser spectroscopy.[4] It remains to be seen whether these many-body potentials can reproduce the VRT *dynamics* in these systems, however.

The work presented here has also demonstrated that none of the water dimer potentials examined so far - considered the best available - is capable of describing the tunneling dynamics or intermolecular vibrations observed by high resolution spectroscopy at an acceptable level of accuracy. Hence, there is a clear motivation to determine a new IPS for the water dimer by least squares inversion of VRT data, as has been accomplished for simpler systems.[12,5,13] Such efforts will be greatly facilitated by the SWPS formulation presented here.

ACKNOWLEDGMENTS

[1] *van der Waals Clusters II*, edited by J. Michl, special thematic issue [Chem. Rev. **94**, 1975 (1994)].

[2] R. J. Saykally and G. A. Blake, Science **259**, 1570 (1993).

[3] J. M. Hutson, Annu. Rev. Phys. Chem. **41**, 123 (1990).

[4] K. Liu, J. Cruzan, and R. J. Saykally, Science **271**, 877 (1996).

[5] M. J. Elrod and R. J. Saykally, J. Chem. Phys. **103**, 933 (1995).

[6] R. C. Cohen and R. J. Saykally, Annu. Rev. Phys. Chem. **42**, 369 (1991).

[7] E. Olthof, A. van der Avoird, P. E. S. Wormer, J. G. Loeser, and R. J. Saykally, J. Chem. Phys. **101**, 921 (1994).

[8] A. C. Peet and W. Yang, J. Chem. Phys. **90**, 1746 (1989).

[9] A. C. Peet and W. Yang, J. Chem. Phys. **91**, 6598 (1989).

[10] W. Yang, A. C. Peet, and W. H. Miller, J. Chem. Phys. **91**, 7537 (1989).

[11] R. C. Cohen and R. J. Saykally, J. Phys. Chem. **94**, 7991 (1990).

[12] R. C. Cohen and R. J. Saykally, J. Chem. Phys. **98**, 6007 (1993).

[13] C. A. Schmuttenmaer, R. C. Cohen, and R. J. Saykally, J. Chem. Phys. **101**, 146 (1994).

[14] R. E. Miller, D. F. Coker, and R. O. Watts, J. Chem. Phys. **82**, 3554 (1985).

[15] D. F. Coker and R. O. Watts, J. Chem. Phys. **91**, 2513 (1987).

[16] M. Quack and M. A. Suhm, J. Chem. Phys. **95**, 28 (1991).

[17] J. K. Gregory and D. C. Clary, Chem. Phys. Lett. **228**, 547 (1994).

[18] V. Buch, J. Chem. Phys. **97**, 726 (1992).

[19] M. D. Feit, J. D. Fleck, and A. Steiger, J. Comput. Phys. **47**, 412 (1982).

[20] M. D. Feit and J. D. Fleck, J. Chem. Phys. **78**, 301 (1983).

[21] D. Kosloff and R. Kosloff, J. Comput. Phys. **52**, 35 (1983).

[22] R. Kosloff and D. Kosloff, J. Chem. Phys. **79**, 1823 (1983).

[23] R. Kosloff, J. Phys. Chem. **92**, 2087 (1988).

[24] R. Friesner, J. Bentley, M. Menou, and C. Leforestier, J. Chem. Phys. **99**, 324 (1993).

[25] Z. Bačić and J. C. Light, J. Chem. Phys. **85**, 4594 (1986).

[26] Z. Bačić and J. C. Light, J. Chem. Phys. **87**, 4008 (1987).

[27] R. Friesner, J. Chem. Phys. **85**, 1462 (1985).

[28] J. Antikainen, R. Friesner, and C. Leforestier, J. Chem. Phys. **102**, 1270 (1995).

[29] G. Corey and D. Lemoine, J. Chem. Phys. **97**, 4115 (1992).

[30] J. C. Light, I. P. Hamilton, and J. V. Lill, J. Chem. Phys. **82**, 1400 (1985).

[31] M. J. Bramley, J. W. Tromp, T. Carrington, and G. C. Corey, J. Chem. Phys. **100**, 6175 (1994).

[32] C. Leforestier, J. Chem. Phys. **101**, 7357 (1994).

[33] D. Lemoine, J. Chem. Phys. **101**, 10526 (1994).

[34] O. A. Sharafeddin and J. C. Light, J. Chem. Phys. **102**, 3622 (1995).

[35] G. Corey and J. W. Tromp, J. Chem. Phys. **103**, 1812 (1995).

[36] C. Lanczos, J. Res. Natl. Bur. Stand. **45**, 255 (1950).

[37] J. K. Cullum and R. A. Willoughby, *Lanczos Algorithms for Large Symmetric Eigenvalues Computations* (Birkhäuser, Boston, 1985).

[38] T. R. Dyke, J. Chem. Phys. **66**, 482 (1977).

[39] N. Pugliano, J. D. Cruzan, J. G. Loeser, and R. J. Saykally, J. Chem. Phys. **98**, 6600 (1993).

[40] J. T. Hougen, J. Mol. Spectrosc. **114**, 395 (1987).

[41] L. H. Coudert and J. T. Hougen, J. Mol. Spectrosc. **139**, 250 (1990).

[42] T. R. Dyke and J. S. Muenter, J. Chem. Phys. **60**, 2929 (1974).

[43] T. R. Dyke, K. M. Mack, and J. S. Muenter, J. Chem. Phys. **66**, 498 (1977).

[44] J. A. Odutula and T. R. Dyke, J. Chem. Phys. **72**, 5062 (1980).

[45] T. R. Dyke, in *Structure and Dynamics of Weakly Bound Molecular Complexes*, edited by A. Weber (Reidel, Boston, 1987), p. 43.

[46] J. T. A. Hu, D. Prinslow, S. E. O'Dell, and T. R. Dyke, J. Chem. Phys. **88**, 5352 (1988).

[47] L. H. Coudert, F. J. Lovas, R. D. Suenram, and J. T. Hougen, J. Chem. Phys. **87**, 6290 (1987).

[48] L. Martinache, S. Jans-Bürli, B. Vogelsanger, W. Kresa, and A. Bauder, Chem. Phys. Lett. **149**, 424 (1988).

[49] T. A. Hu and T. R. Dyke, J. Chem. Phys. **91**, 7348 (1989).

[50] R. D. Suenram, G. T. Fraser, and F. J. Lovas, J. Mol. Struct. **138**, 440 (1990).

[51] E. N. Karyakin, G. T. Fraser, and R. D. Suenram, Mol. Phys. **78**, 1179 (1993).

[52] Z. S. Huang and R. E. Miller, J. Chem. Phys. **88**, 8008 (1988).

[53] Z. S. Huang and R. E. Miller, J. Chem. Phys. **91**, 6613 (1989).

[54] G. T. Fraser, R. D. Suenram, L. H. Coudert, and R. S. Frye, J. Mol. Struct. **137**, 244 (1989).

[55] G. T. Fraser, R. D. Suenram, and L. H. Coudert, J. Chem. Phys. **90**, 6077 (1989).

[56] K. L. Busarow, R. C. Cohen, G. A. Blake, K. B. Laughlin, Y. T. Lee, and R. J. Saykally, J. Chem. Phys. **90**, 3937 (1989).

[57] E. Zwart, J. Muelen, and W. L. Meerts, Chem. Phys. Lett. **166**, 500 (1990).

[58] E. Zwart, J. Muelen, W. L. Meerts, and L. H. Coudert, J. Mol. Struct. **147**, 27 (1991).

[59] N. Pugliano and R. J. Saykally, J. Chem. Phys. **96**, 1832 (1992).

[60] G. T. Fraser, Int. Rev. Phys. Chem. **10**, 189 (1991).

[61] R. J. Saykally *et al.* (unpublished).

[62] M. Lewerenz and R. O. Watts, J. Chem. Phys (in press).

[63] J. R. Reimers, R. O. Watts, and M. L. Klein, Chem. Phys. **64**, 95 (1982).

[64] J. K. Gregory and D. C. Clary, J. Chem. Phys. **103**, 8924 (1995).

[65] C. Millot and A. J. Stone, Mol. Phys. **77**, 439 (1992).

[66] S. C. Althorpe and D. C. Clary, J. Chem. Phys. **101**, 3603 (1994).

[67] S. C. Althorpe and D. C. Clary, J. Chem. Phys. **102**, 4390 (1995).

[68] B. J. Smith, D. J. Swanton, J. A. Pople, H. F. Schaefer, and L. Radom, J. Chem. Phys. **92**, 1240 (1990).

[69] S. S. Xantheas and T. H. Dunning, J. Chem. Phys. **100**, 7523 (1994).

[70] O. Matsuoka, E. Clementi, and M. Yoshimine, J. Chem. Phys. **64**, 1351 (1976).

[71] J. K. Gregory and D. C. Clary, J. Chem. Phys. **105**, 6626 (1996).

[72] G. Brocks, A. der Avoird, B. T. Sutcliffe, and J. Tennyson, Mol. Phys. **50**, 1025 (1983).

[73] C. Leforestier, J. Chem. Phys. **94**, 6388 (1991).

[74] N. Halberstadt (private communication).

[75] W. Rijks and P. E. S. Wormer, J. Chem. Phys. **90**, 6507 (1989).

[76] W. Rijks and P. E. S. Wormer, J. Chem. Phys. **92**, 5754 (1990).

[77] M. M. Szczesniak, R. J. Brenstein, S. M. Cybulski, and S. Scheiner, J. Phys. Chem. **94**, 1781 (1990).

[78] J. K. Gregory and D. C. Clary, J. Phys. Chem., **103**, 8924 (1996).